Measurement of the acoustic velocity field of nonlinear standing waves using the synchronized PIV technique

Majid Nabavi *, Kamran Siddiqui, Javad Dargahi

Department of Mechanical and Industrial Engineering, Concordia University, 1455 de Maisonneuve Blvd, West Montreal, Quebec, Canada H3G 1M8

ABSTRACT

The motion of gas within an air-filled rigid-walled square channel subjected to acoustic standing waves is experimentally investigated. The synchronized particle image velocimetry (PIV) technique has been used to measure the acoustic velocity fields at different phases over the excitation signal period. The acoustic velocity measurements have been conducted for two different acoustic intensities in the quasi-nonlinear range (in which the nonlinear effects can be neglected in comparison with the dissipation effects), and one acoustic intensity in the finite-amplitude nonlinear range (in which both the nonlinear term and the dissipative term play a role in the wave equation). The experimental velocity fields for the quasi-nonlinear cases are compared with the analytical results obtained from the time-harmonic solution of the wave equation. Good agreement between the experimental and analytical velocity fields proves the ability of the synchronized PIV technique to accurately measure both temporal and spatial variations of the acoustic velocity fields. The verified technique is then used to measure the acoustic velocity fields of the finite-amplitude nonlinear case at different phases.

© 2008 Elsevier Inc. All rights reserved.

1. Introduction

The study of nonlinear acoustic standing waves in closed tubes is very important in the design of a wide range of systems such as thermoacoustic devices [1,2], high quality resonators [3], standing wave motors [4] and particle filtration and levitation equipment [5]. When a standing wave is induced in a tube, the shape and amplitude of pressure and particle velocity inside the tube are strongly dependent on the amplitude of the excitation signal. Although several papers dealing with the analytical [6–8] and numerical [3,9–13] studies of nonlinear standing waves, as well as experimental investigation of the acoustic pressure in the nonlinear standing wave tube [14,15] can be found in the literature, relatively few experimental investigations have been performed to measure the acoustic velocity fields inside a standing wave resonator.

The acoustic particle velocity can be measured using different techniques. Huelsz et al. [16,17] used hot-wire anemometry (HWA) to measure acoustic velocities in the linear range (maximum velocity of 0.8 m/s). Laser Doppler anemometry (LDA) has also been used to measure acoustic velocity. Vignola et al. [18] assembled and tested a differential LDA to provide noninvasive measurements of the acoustic velocities of linear standing waves

generated in a water-filled tube. Thompson et al. [19] used LDA with burst spectrum analysis (BSA) to study the acoustic velocities of amplitude less than 1.3 m/s (linear range) generated in a cylindrical standing-wave resonator filled with air. Gazengel et al. [20] assessed the performances of two LDA systems adapted for measuring the acoustic particle velocities in an enclosed acoustic field. This assessment was performed by comparing the acoustic velocities measured by means of LDA to reference acoustic velocities estimated from sound pressure measurements. In their experiments, the maximum velocity amplitudes were 0.1, 1 and 10 mm/s (linear range) and the corresponding relative errors were 11%, 5% and 3.6%. These techniques however, provide velocity measurements at a point in space, therefore, detailed simultaneous two-dimensional flow structure cannot be obtained from these techniques. Furthermore, HWA is an intrusive technique which disturbs the velocity fields inside the resonator.

PIV provides two-dimensional velocity fields with high spatial resolution. PIV is used routinely in many experimental investigations of fluid flows and heat transfer [21,22]. However, very few studies have reported the velocity measurements of the acoustic standing wave using PIV. Hann and Greated [23,24] have shown the ability of PIV to measure the amplitude of the sinusoidal sound field and the mean flow. They measured particle velocities of an acoustic standing wave inside a square channel at a frequency of 1616 Hz. However, they did not present detailed velocity characteristics. Campbell et al. [25] reported a review of PIV with its application to the measurement of sound. Shin et al. [26] used

* Corresponding author. Tel.: +1 514 8482424x7102; fax: +1 514 8483175.
  E-mail address: m_nabav@encs.concordia.ca (M. Nabavi).

PIV to study the velocity field in the acoustic boundary layer of a linear standing wave in liquid within a small tube of 315 mm length and 3 × 3 mm cross-section. In their experiment, the velocity fields were measured at different temporal values with respect to the driving sinusoidal signal using a set of delay generators. However, their experiment was performed in the linear range of acoustic intensity and they measured the velocity field in a small field of view (190 × 150 μm) near the wall in order to investigate the boundary layer effect. Recently, Castrejón-Pita et al. [27] used PIV and LDA to measure amplitude and phase of velocity on the laminar oscillatory viscous boundary layer produced by an acoustic standing wave. They found a good agreement between the experimental data and the predictions made by the Rayleigh viscous boundary layer theory.

As the literature review indicates, all previous studies related to the acoustic velocity measurement have been performed in the linear range and consequently, no experimental study has reported the spatial and temporal variations of the velocity field inside a nonlinear acoustic standing wave resonator. Some of the challenges of taking accurate PIV measurements in the nonlinear standing wave resonator are (1) using a synchronized technique to measure the velocity field at different phases, (2) choosing the appropriate separation time between two images based on the excitation frequency and acoustic intensity magnitude, to accurately measure large-gradient, high-frequency nonlinear velocity fields, and (3) using a proper particle image processing algorithm for the improvement of PIV velocity measurements characterized by large velocity gradients.

In the present study, we investigated the behavior of the acoustic velocity fields of nonlinear standing waves temporally and spatially using the synchronized PIV technique. We have first applied the technique to two cases in which the nonlinear effects can be neglected in comparison with the dissipation effects. Therefore, the resultant wave equation can be solved analytically. The analytical formula for the particle velocity variations can be used to compare with the experimental velocities. After the validation, the technique is used for the finite-amplitude nonlinear velocity measurement in which both the nonlinear term and the dissipative term play a role in the wave equation. To the best of the authors' knowledge, this work is the first experimental investigation of the spatial and temporal particle velocity inside a nonlinear acoustic standing wave tube.

2. Synchronized PIV technique

In the PIV technique, a laser light sheet is pulsed twice with a known time separation between the two pulses. A CCD camera captures the images of the tracer particles at each pulse in the flow field of interest. The displacement of particles between the two images divided by the time separation between the laser pulses provides the velocity field. In the conventional PIV setup, the laser pulses are synchronized with the camera frames. Typically these signals are not synchronized with any flow characteristics, as for steady flows this is not necessary. However, for velocity measurements in the presence of an acoustic standing wave, these signals should be synchronized with the excitation signal to capture the velocity fields at the desired phase. We developed an electronic circuit to generate a trigger signal which synchronizes the laser pulses and camera frame with any particular phase of the excitation signal. This phase can be adjusted from 0 to 2π and therefore, covers the whole period of the excitation waveform. Since the time delay, width of the trigger signal, frequency of the excitation signal and time separation between two laser pulses are accurately known, the phase where two laser pulses are located in the excitation signal can be computed.

3. Experimental setup

The schematic of the experimental setup developed to measure the acoustic velocity fields inside the standing wave tube using the synchronized PIV technique is shown in Fig. 1. The acoustic
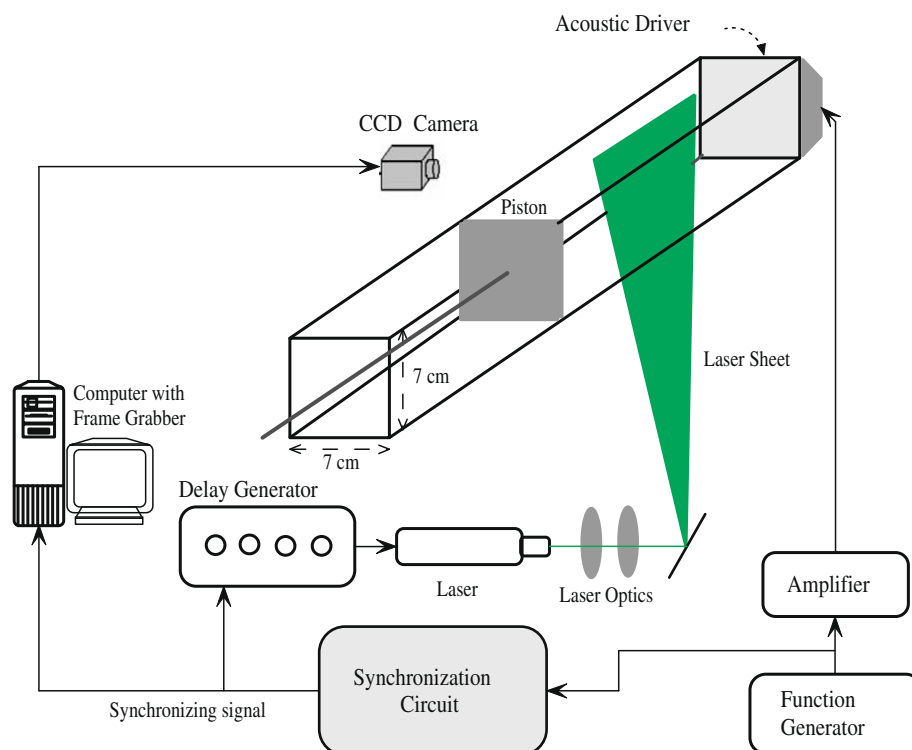

Fig. 1. Schematic of the experimental setup and instrumentation.

chamber is a Plexiglas channel with a square cross-sectional area. The inner dimensions of the channel are 7 cm × 7 cm. The walls of the channel are 6 mm thick, and therefore, the assumption of rigid walls held for this channel. The two-dimensional velocity fields inside the channel are measured using synchronized PIV. The measurements are made in a plane parallel to the channel length at the mid-channel location as shown in Fig. 1. A 120 mJ Nd:YAG laser (Solo PIV 120XT, New Wave Research) is used as a light source for the PIV measurements. A CCD camera (JAI, CV-M2) with the resolution of 1600 × 1200 pixels is used to image the flow. The camera is connected to a PC equipped with a frame grabber (DVR Express, IO Industries, London, ON, Canada) that acquires 8 bit images at a rate of 30 Hz. A four-channel digital delay generator (555-4C, Berkeley Nucleonics Corporation, San Rafael, CA) is used to control the timing of the laser pulses. BIS(2-ETHYLHEXYL) SEBACATE mist with the mean diameter of 0.5 μm is used as the tracer particles. An aerosol generator (Lavision Inc., Ypsilanti, MI) is used to generate the mist. A special loudspeaker driver is used to excite the acoustic standing wave inside the tube. The driver has a maximum power of 200 watts and DC resistance of 8Ω. The use of a loudspeaker driver as an acoustic source made it easy to vary the frequency and intensity of excitation continuously and precisely. A function generator (model Agilent 33120A) is used to generate the sinusoidal waves of different frequencies and amplitudes. The accuracy of the generated frequency and amplitude are 1 μHz and 0.1 mV, respectively. The signal from the function generator is amplified by a 220-W amplifier (Pioneer SA-1270). The loudspeaker is driven by this amplified signal (see Fig. 1). The driver frequency (f) is set equal to 935 Hz. The corresponding wavelength (λ) of the acoustic standing wave is 36.4 cm. The length of the channel (L) is adjusted with the movable piston to allow the formation of two full standing waves inside the channel (i.e. $L = 2\lambda = 72.8$ cm). Before conducting PIV measurements, the duct's length is tuned to get the appropriate resonance. The field of view of the CCD camera is set in a way to map the flow field in the half wavelength section. That is, the field of view of the camera is set equal to 19 cm in horizontal and 14.25 cm in vertical. In order to accurately measure the periodic particle velocity, the separation time between two images must be adjusted appropriately. Due to the oscillation of the particles, the time separation between the two images of an image pair should be much less than a quarter of the wave period. Otherwise, the particle displacement computed by cross-correlating the PIV images will be smaller than the actual displacement of the particles. This will result in underestimating the acoustic velocities. On the other hand, for a very short separation time, the particle shift between images of an image pair will be too small and will increase uncertainty in the velocity measurements. In the present case, the time separation is set equal to 40 μs, which is about seven times smaller than the quarter of wave period. The vertical dimension of the camera field of view is larger than the channel height. Therefore, before computing the velocity vectors, the images are preprocessed to remove the regions outside the channel from the images. A non-commercial computer code is used for PIV velocity computation by cross-correlating the interrogation region in the first image with the corresponding search region in the second image. The size of the interrogation region is set equal to 32 × 32 pixels and the size of the search region is set equal to 64 × 64 pixels. A three-point Gaussian sub-pixel fit scheme is used to obtain the correlation peak with sub-pixel accuracy. A 50% window overlap is used in order to increase the nominal resolution of the velocity field to 16 × 16 pixels. This resulted in a spatial resolution of 1.9 × 1.9 mm of the velocity field. A scheme is used to identify the spurious velocity vectors and then correct them using a local median test [28].

The maximum diaphragm velocity is also measured for each excitation amplitude. A Brüel & Kjær laser vibrometer is used to
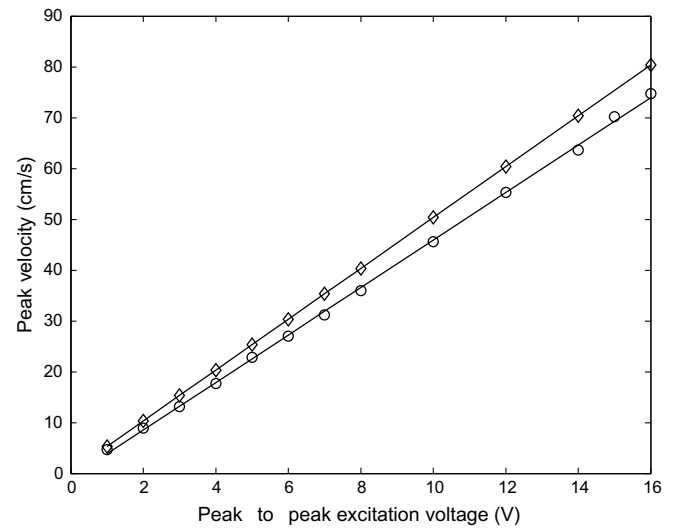

Fig. 2. Maximum velocity at the center of the driver diaphragm (u_0) versus excitation voltage at different excitation frequencies; ○, 496 Hz; ◇, 1020 Hz; Solid line, linear fit. The overall bias error between the measured and fitted velocities for f = 496 and 1020 Hz is 0.36 and 0.49 cm/s, respectively.

measure this parameter. The laser vibrometer consists of three components: A Helium–Neon laser velocity transducer type 8323, a power supply type 2815 and a signal analyzer unit type 2035. Unlike traditional contact vibration transducers, the laser vibrometer requires no physical contact with the test object. The measurement principle of a laser vibrometer is based on the Doppler Effect. When monochromatic laser light is scattered back from a vibrating target it undergoes a frequency shift proportional to the velocity of the target. Fig. 2 shows the maximum vibration velocity at the center of the driver's diaphragm (u_0) as a function of the excitation voltage of the driver for different excitation frequencies. The plot shows that for a given excitation frequency, the diaphragm velocity and excitation voltage are almost linearly related. The plot also shows that the slope increases with the excitation frequency. With the use of Fig. 2, at a given excitation frequency, the amplitude of diaphragm velocity can be estimated at all excitation voltages over the range of our practical interest. To confirm that the assumption of rigid walls holds for the channel used in this study, we have also measured the wall vibration using the laser vibrometer. The maximum wall displacement is found to be approximately 0.5 μm which is about 0.5% of the maximum displacement of the acoustic driver which is around 100 μm. To confirm that the speaker was not saturated particularly at high amplitudes, the spectra of the laser vibrometer output signal were analyzed. The results showed a peak at the excitation frequency with an amplitude significantly higher than the adjacent frequencies, which confirms that the speaker was not saturated. By adjusting the time delay in the synchronization circuit, the measurements are taken at 18 different phases of the excitation signal. The first image is taken at the desired phase. For each phase of the excitation voltage, 200 PIV images are captured. From these images, 100 acoustic velocity fields are computed.

4. Mathematical formulation

The description of nonlinear acoustic waves in a viscous, heat-conducting fluid is obtained using the basic equations of fluid mechanics along with the appropriate state equation which can be written in one-dimension as

Continuity equation:

$$\rho_t + (\rho u)_x = 0, \tag{1}$$

Navier-Stokes equation:

$$\rho\left(u_t + \frac{1}{2}(u^2)_x\right) = -p_x + \left(\mu_B + \frac{4}{3}\mu\right)u_{xx}, \tag{2}$$

where u is the axial acoustic velocity, ρ and p are density and pressure, respectively, which can be written as $\rho = \rho_0 + \rho'$ and $p = p_0 + p'$, where prime denotes perturbation in the given parameter and subscript "0" represents the static value, μ and μ_B are the shear and bulk viscosities, respectively.

State equation: An equation of state particularly useful in acoustic is one that relates pressure to density and entropy i.e., $p = p(\rho, s)$,

$$p' = \left(\frac{\partial p}{\partial \rho}\right)_s \rho' + \left(\frac{\partial p}{\partial s}\right)_\rho s'. \tag{3}$$

Using $\rho_0 T_0 \frac{\partial s'}{\partial t} = \kappa T'_{xx}$ (where $T' = \left(\frac{\partial T}{\partial p}\right)_s p'$, and κ is the coefficient of thermal conduction), and the simplified version of the momentum equation, $\rho_0 \partial u/\partial t = -p'_x$, it can be obtained, $s' = -\frac{\kappa}{T_0}\left(\frac{\partial T}{\partial p}\right)_s u_x$, and using,

$\frac{1}{T_0}\left(\frac{\partial p}{\partial s}\right)_\rho \left(\frac{\partial T}{\partial p}\right)_s = \frac{1}{c_V} - \frac{1}{c_p}$, it can be written,

$$\left(\frac{\partial p}{\partial s}\right)_\rho s' = -\kappa\left(\frac{1}{c_V} - \frac{1}{c_p}\right)u_x, \tag{4}$$

where c_p and c_V are the specific heats at constant pressure and constant volume. Regarding the first term on the right-hand side of Eq. (3), the sound speed c can be introduced as

$$c^2 \equiv (\partial p/\partial \rho)|_{s=\text{const}}. \tag{5}$$

The sound speed may be thought of as a new thermodynamic variable, since it is derived from other thermodynamic quantities. For finite-amplitude nonlinear case ($|\rho'| \ll \rho_0$), c^2 becomes constant, which can be denoted as c_0^2. Thus, a modified equation of state in one-dimension can be written as [29,13]

$$p' = c_0^2 \rho' - \kappa\left(\frac{1}{c_V} - \frac{1}{c_p}\right)u_x. \tag{6}$$

Assuming $|\rho'| \ll \rho_0$, the one-dimensional finite-amplitude nonlinear wave equation in a thermoviscous fluid can be derived using Eqs. (1), (2), and (6), and written as

$$u_{tt} - c_0^2 u_{xx} = \left(vbu_{tx} - \frac{1}{2}(u^2)_t\right)_x, \tag{7}$$

where v is the kinematic viscosity and b indicates the total effect of viscosity and thermal conductivity of the fluid as well as the wall absorption. This can be written as

$$b = \frac{2c_0^3\alpha}{\omega^2 v}, \tag{8}$$

where $\omega = 2\pi f$ and α is the total absorbtion coefficient which is the sum of thermoviscosity absorbtion coefficient and wall absorbtion coefficient [30]. α is expressed as

$$\alpha = \alpha_{tv} + \alpha_{wall},$$
$$\alpha_{tv} = \frac{\omega^2 v}{2c_0^3}\left(\frac{4}{3} + \frac{\mu_B}{\mu} + \frac{\gamma-1}{Pr}\right),$$
$$\alpha_{wall} = \sqrt{\frac{\omega v}{8c_0^2}}\left(1 + \frac{\gamma-1}{\sqrt{Pr}}\right)\frac{\wp}{\Lambda}, \tag{9}$$

where $Pr = \frac{\mu c_p}{\kappa}$ is the Prandtl number, Λ is the cross-sectional area, $\gamma = c_p/c_V$ is the ratio of specific heats, and $\wp$ is the perimeter of the resonator [30].

Both the nonlinear term ($\frac{1}{2}(u^2)_t$) and dissipative term (vbu_{tx}) in the righthand side of Eq. (7) play a role in the deviation of the velocity from the pure sinusoidal waveform observed in the linear standing wave. Under certain condition (which will be discussed

later in this section), the nonlinear term can be neglected in comparison with the dissipative term. Thus, Eq. (7) can be simplified as

$$u_{tt} - c_0^2 u_{xx} - vbu_{txx} = 0. \tag{10}$$

We call this equation the *quasi-nonlinear* wave equation to differentiate it from the finite-amplitude nonlinear case (Eq. (7)) and linear wave equation in lossless medium ($u_{tt} = c_0^2 u_{xx}$).

The fluid is excited by the harmonic motion of a diaphragm at $x = 0$ at the frequency f. Assuming L to be the length of the tube (equal to 2λ in the present case), the following boundary conditions are applicable,

$$u(0,t) = u_0\cos(wt), \quad u(L,t) = 0. \tag{11}$$

A solution of the form $u(x,t) = U(x)e^{-j\omega t}$ is sought for Eq. (10). We write,

$$U'' + \frac{\omega^2}{c_0^2 - jvb\omega}U = 0. \tag{12}$$

Defining the dissipation parameter $\delta \equiv \frac{vb\omega}{2c_0^2}\frac{\omega L}{c_0} \ll 1$ [8], we get,

$$U'' + \left(\frac{\omega}{c_0}\left(1 + j\frac{c_0}{\omega L}\delta - \frac{3c_0^2}{2\omega^2 L^2}\delta^2\right)\right)^2 U = 0. \tag{13}$$

Solving Eq. (13) and using the boundary conditions (11) we obtain,

$$u(x,t) = \frac{u_0}{(1 + \frac{\delta^2}{2})\sin^2\frac{\omega' L}{c_0} + \delta^2\cos^2\frac{\omega' L}{c_0}}$$
$$\times\left(\left[\left(1 + \frac{\delta^2(L-x)^2}{2L^2}\right)\sin\frac{\omega' L}{c_0}\sin\frac{\omega'(L-x)}{c_0}\right.\right.$$
$$\left.+\delta^2\frac{L-x}{L}\cos\frac{\omega' L}{c_0}\cos\frac{\omega'(L-x)}{c_0}\right]\cos\omega t$$
$$+\delta\left[\frac{L-x}{L}\sin\frac{\omega' L}{c_0}\cos\frac{\omega'(L-x)}{c_0} - \cos\frac{\omega' L}{c_0}\sin\frac{\omega'(L-x)}{c_0}\right]$$
$$\left.\times\sin\omega t\right), \tag{14}$$

where $\omega' = \omega\left(1 - \frac{3c_0^2\delta^2}{2\omega^2 L^2}\right)$.

Eq. (14) represents the analytical solution for the one-dimensional acoustic velocity of quasi-nonlinear case. In order to find the condition when Eq. (10) (from which Eq. (14) is obtained) is valid, we estimate the nonlinear and dissipative terms on the right-hand side of Eq. (7). Assuming $\delta \ll 1$, we can write,

$$u(x,t) \simeq \left(u_0\sin\frac{\omega'(L-x)}{c_0}\bigg/\sin\frac{\omega' L}{c_0}\right)\cos\omega t.$$

It is found that $\frac{1}{2}(u^2)_t \sim \omega u_0^2$, and $vbu_{tx} \sim v\,bu_0\omega^2/c_0$. Therefore, the condition when nonlinear effects can be neglected in comparison with dissipation effects can be found as, $\eta \equiv \frac{u_0 c_0}{vb\omega} \ll 1$. This condition can be written in terms of the acoustical Reynolds number ($Re = c_0 u_{max}/bv\omega$) as

$$Re \ll \frac{u_{max}}{u_0}. \tag{15}$$

where u_{max} is the maximum acoustic velocity. Therefore, as long as the acoustic intensity is not very intense so that Eq. (15) is satisfied, we can consider Eq. (14) as a valid solution for the finite-amplitude nonlinear wave in an enclosure. Acoustical Reynolds number is a non-dimensional parameter used to quantify the nonlinearity of the acoustic wave. The acoustic waves are considered to be linear if Re is sufficiently less than unity. However, nonlinear acoustical theory must be used when the amplitude of the oscillations of the medium is sufficiently great, so that Re is of the order of unity or higher [8].
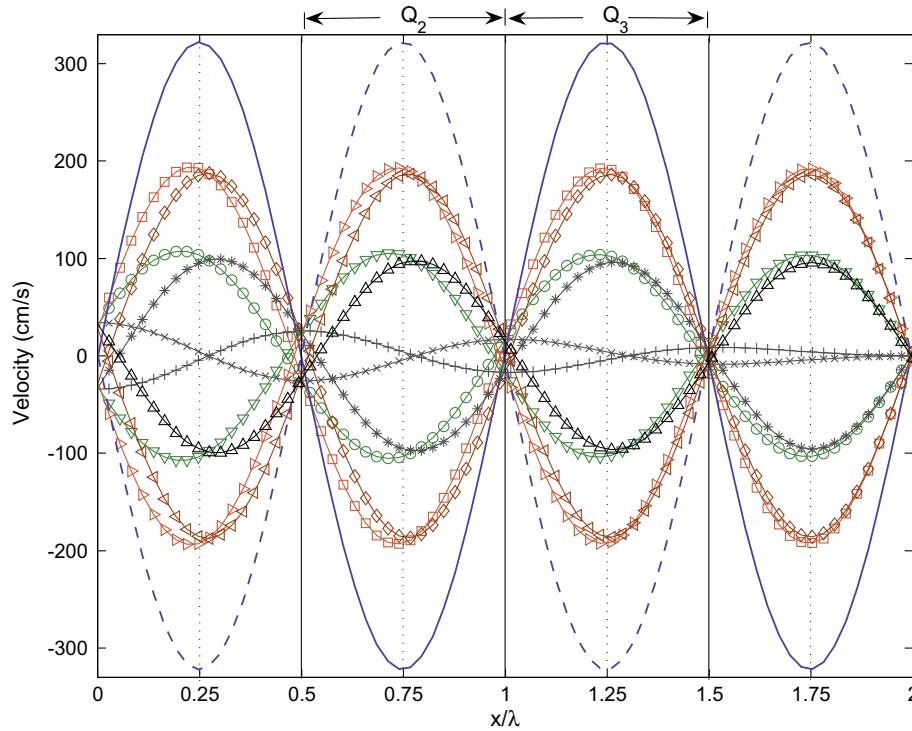
Fig. 3. The axial variation of the analytical axial velocity for $u_0 = 34$ cm/s at different phases: $t/T = 0$, ×; $t/T = 0.05$, ○; $t/T = 0.1$, □; $t/T = 0.25$, solid line; $t/T = 0.4$, ◇; $t/T = 0.45$, ∗; $t/T = 0.5$, +; $t/T = 0.55$, ▽; $t/T = 0.6$, ▷; $t/T = 0.75$, dashed line; $t/T = 0.9$, ◁; $t/T = 0.95$, △.

The axial distribution of the analytical axial velocity (Eq. (14)) over the entire tube for $u_0 = 34$ cm/s at different phases is plotted in Fig. 3. The phases at which the velocity was plotted are $t/T = 0$, 0.05, 0.1, 0.25, 0.4, 0.45, 0.5, 0.55, 0.6, 0.75, 0.9, and 0.95. As expected the maximum velocity at the vibrator end is u_0 and at the other end is zero. The variation of the velocity fields especially near the vibrator end and when the velocity magnitude is low, are deviated from the pure sinusoidal waveform.

5. Results and discussion

All experiments are conducted in air at 20 °C. The static pressure inside the tube is atmospheric. The thermo-physical properties of air at this condition are, $c_0 = 340.6$ m/s, $\rho_0 = 1.2$ kg/m^3, $\mu = 1.81 \times 10^{-5}$ N s/m^2, $\mu_B = 0.6 \times \mu$ and $\gamma = 1.401$. The first set of experiments has been performed for the quasi-nonlinear condition. The reason is that the analytical solution for the quasi-nonlinear case is available (Eq. (14)) and thus, the experimental results can be compared with the analytical ones in order to validate the measured data. The results are presented for two excitation amplitudes that correspond to the maximum diaphragm velocity (u_0) of 34 and 40 cm/s, hereinafter referred to as cases A and B, respectively. The maximum acoustic velocity for cases A and B is approximately 3.2 and 3.8 m/s, respectively. Thus, the acoustical Reynolds number is 0.57 for case A and 0.66 for case B, which lie in the quasi-nonlinear range. For both cases, $u_{max}/u_0 = 9.5$, which implies that for the validity of Eq. (14), we must have $Re \ll 9.5$, which is true for both cases. Therefore, we conclude that the validation condition (Eq. (15)) is satisfied and Eq. (14) is a valid solution for both cases.

The experimental velocity vectors along with the transversely averaged axial velocities for cases A and B are shown in Figs. 4 and 5 at four different phases. The measurements have been done over the second half-wavelength (Q_2 in Fig. 3) for case A and over the third half-wavelength (Q_3 in Fig. 3) for case B. Two steps were taken to obtain the transversely averaged axial velocities. First, the average two dimensional velocity field is obtained first by averaging 100 PIV fields i.e. average velocity is computed at each grid point. In the next step, at each axial location, the axial velocities are transversally averaged. The corresponding axial velocities obtained from the analytical formula (Eq. (14)) are also plotted for comparison. A good agreement in both shape and amplitude between the experimental and analytical values of the axial velocity along the channel is observed at all phases for both cases. At all phases (especially the phases at which the velocity amplitude is low), the velocity profiles differ from a perfect sinusoidal wave field which is expected due to attenuation caused by viscous and nonlinear effects. At phases that correspond to the lower velocity magnitudes, i.e. $t/T = 0.476$ and 0.980 (see Figs. 4b and d and 5b and d), it is observed that the maximum and minimum peaks are not located at the middle of the Q_2 and Q_3 sections, rather they are shifted slightly in the direction away from the driver end.

Furthermore, as shown in Figs. 4, and 5, the peaks of the experimental and analytical data at all phases are almost coincident, indicating that these phase-dependent shifts are also predicted by the mathematical solution of the quasi-nonlinear case. As shown in Fig. 3, the peaks of velocity at, for example, $t/T = 0.05$ do not occur at $x/\lambda = 0.75$ and 1.25. These phase-dependent shifts are not predicted by the linear wave equation in lossless medium. Aktas et al. found similar shapes for the axial velocity at different phases using a numerical model (see Fig. 2a in [9]).

The difference between the experimental transversely averaged velocity (Ue) and the analytical velocity (Ua) at any particular phase is compared in terms of the relative error (e) defined as

$$e = \frac{e_{\text{bias}}}{u_{\text{m}}}, \quad e_{\text{bias}} = \frac{1}{N} \sum_{i=1}^{N} |Ue_i - Ua_i|, \quad (16)$$
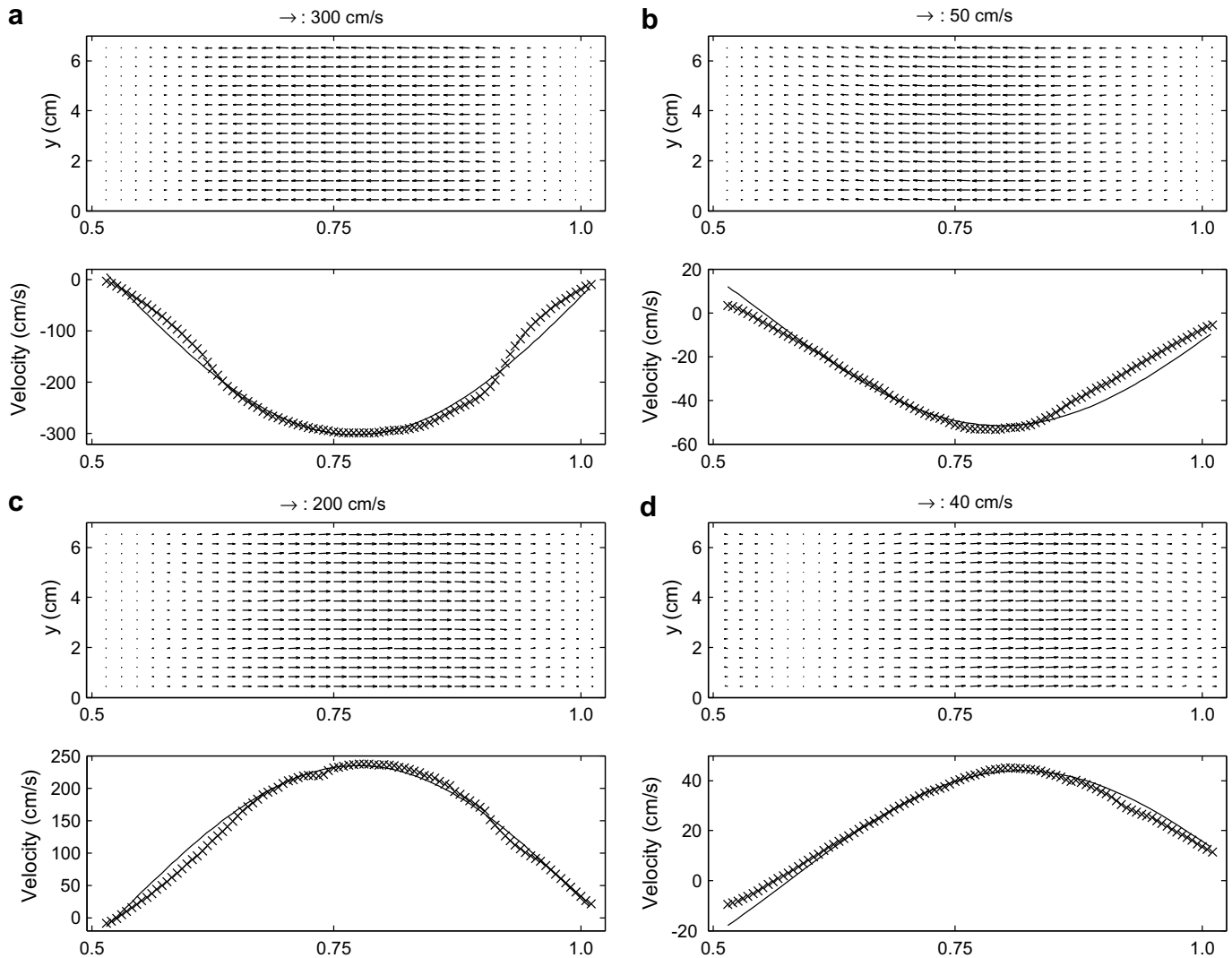
Fig. 4. Particle velocities at $u_0 = 34$ cm/s at four different phases, (a) $t/T = 0.308$, (b) $t/T = 0.476$, (c) $t/T = 0.868$, (d) $t/T = 0.980$; (top) two-dimensional velocity field from PIV measurements, (bottom) corresponding transversely averaged axial velocity ($\times$). The analytical axial velocities are also plotted with solid line. Horizontal axis is x/λ, measured from the driver end. Note that the resolution of the velocity vectors was reduced in the plot for better visualization.

where e_{bias} is the mean of the deviations between the measured and analytical velocities, N is the number of data points in the axial direction and u_m is the maximum magnitude of the analytical axial velocity at that particular phase. In order to obtain the uncertainty in the experimental transversely averaged velocities, we use the average of the standard deviation (mstd) defined by

$$\text{mstd} = \frac{1}{N} \sum_{i=1}^{N} \text{std}_i, \quad \text{std}_i = \sqrt{\frac{1}{M} \sum_{j=1}^{M} (Ue_{i,j} - Ue_i)^2} \tag{17}$$

where M is the number of measured velocity fields at each phase ($M = 100$). The values of relative error e for the axial velocity, e_{bias} for the transversal velocity and mstd for both velocities, at different phases for both cases A and B are presented in Table 1. The results show that the overall relative error of the axial velocity for cases A and B is 7.07% and 7.68%, respectively. At some phases where the amplitude of the axial velocity is high (t/T around 0.25 and 0.75), the relative error is lower than the overall relative error. The overall bias error of the measured transversal velocity is about 1.4 cm/s and 1.6 cm/s for cases A and B, respectively, which is negligible compared to the magnitude of the axial velocity. The differences between the experimental and analytical results for both axial and

transversal velocities are partially related to the existence of the acoustic streaming associated with a standing wave resonator. The streaming velocity is superimposed on the acoustic velocity and its magnitude is much smaller than that of the acoustic velocity. The small values of the uncertainty in the measured axial and transversal velocities indicated by mstd_u and mstd_v in Table 1, show that the experimental transversely averaged velocity are correct.

The synchronized PIV technique enables us to resolve the temporal variation of the particle velocity as well. Fig. 6 shows the temporal variations of the experimental and analytical axial velocities at $x = 3\lambda/4$ (velocity anti-node) and $x = 5\lambda/8$ for case A and $x = 5\lambda/4$ (velocity anti-node) and $x = 9\lambda/8$ for case B. A good agreement is observed between the experimental and analytical results for both cases. The values of the overall relative error (e_t) and the average of the standard deviation (mstd_t) in the temporal variation of the axial velocity over all 18 phases for cases A and B are shown in Table 2. The results show that the relative error is on average 5%.

The acceptable range of differences between the measured and analytical acoustic velocities in both time and space domains proves the ability of the synchronized PIV technique to accurately measure both temporal and spatial acoustic velocities in a nonlinear standing wave tube.
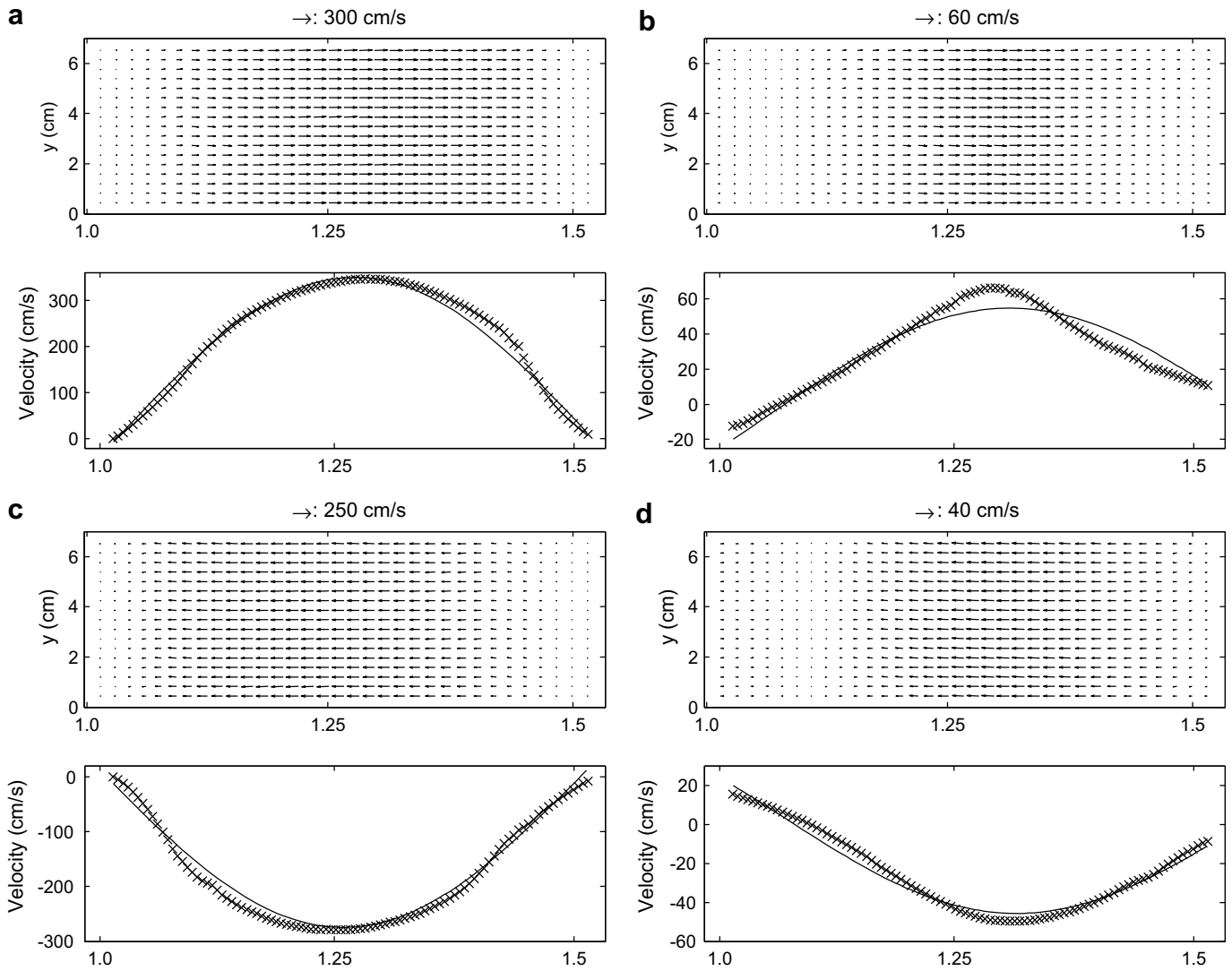
Fig. 5. Particle velocities at $u_0 = 40$ cm/s at four different phases, (a) $t/T = 0.308$, (b) $t/T = 0.476$, (c) $t/T = 0.868$, (d) $t/T = 0.980$; (top) two-dimensional velocity field from PIV measurements, (bottom) corresponding transversely averaged axial velocity ($\times$). The analytical axial velocities are also plotted with solid line. Horizontal axis is x/λ, measured from the driver end. Note that the resolution of the velocity vectors was reduced in the plot for better visualization.

We have presented the results for the quasi-nonlinear cases that have analytical solution in order to compare the experimental data with the theoretical results and validate the accuracy of the measurement technique. In the next set of experiment, we used the verified synchronized PIV technique to measure the acoustic velocity field of finite-amplitude nonlinear standing wave, that is, when both nonlinear and dissipation effects are significant. Fig. 7 shows the axial variation of the particle velocity profile at four different phases. The maximum vibrational amplitude of the driver is $u_0 = 95$ (cm/s). The maximum acoustic velocity (u_{max}) in this case is 7.28 (m/s) and the corresponding Reynolds number is 1.27. Aktas et al. have reported the similar shape for the spatial variation of the acoustic velocity using a numerical scheme (see Fig. 2b in Ref. [9]). Fig. 7 also shows that for the nonlinear case, the velocity peaks move across the resonator with time, whereas they are almost fixed at the middle of the resonator in the linear case. The peak of the wave (where u has its greatest value) travels fastest and the trough (where u is least) travels slowest. Consequently, the peak tends to catch up with the trough [30]. Since in the present case the nonlinearity effects are not very large, a slight shift in the peak locations is observed. The maximum difference between the position of the velocity peaks is about 0.1λ. This difference is

Table 1
Percentage of the relative error for the axial velocity (e_u), bias error for the transversal velocity ($e_{u\ bias}$) and the average of the standard deviation for both velocities (mstd$_u$ and mstd$_v$) in spatial variation at different phases for cases A and B

| t/T	case A				case B			
	e_u (%)	mstd$_u$ (cm/s)	$e_{u\ bias}$ (cm/s)	mstd$_v$ (cm/s)	e_u (%)	mstd$_u$ (cm/s)	$e_{u\ bias}$ (cm/s)	mstd$_v$ (cm/s)
0.028	16.26	2.2	0.51	0.2	15.71	2.9	0.48	0.4
0.084	6.54	0.6	0.60	0.4	9.82	1.1	1.44	0.7
0.140	11.77	1.4	1.07	0.7	7.61	2.7	0.83	0.7
0.196	7.62	1.6	1.01	0.9	3.17	1.4	0.98	0.8
0.252	4.79	1.6	1.38	1.1	4.86	1.9	1.40	1.0
0.308	3.88	1.9	0.86	0.7	3.68	1.5	2.04	0.8
0.364	5.69	2.1	0.95	0.7	6.09	2.0	1.27	0.6
0.420	7.29	2.0	2.78	0.9	9.98	2.0	1.74	0.6
0.476	5.49	1.2	2.13	0.8	7.12	1.6	0.63	0.5
0.532	4.60	0.7	1.02	0.5	9.51	0.7	1.48	0.4
0.588	7.38	0.8	2.07	0.5	7.49	1.4	1.54	0.6
0.644	6.49	1.6	1.88	0.9	7.07	1.6	3.83	0.8
0.700	4.40	2.3	1.76	0.9	3.61	1.9	3.22	1.1
0.756	3.05	2.6	1.43	1.0	6.06	2.2	2.98	1.0
0.812	7.07	2.5	3.05	1.0	8.19	2.7	2.60	0.9
0.868	9.47	2.4	1.3	0.9	8.31	3.5	2.26	1.1
0.924	10.9	1.8	1.21	0.8	12.56	2.3	1.10	0.7
0.980	4.54	0.7	0.52	0.5	6.76	0.5	0.91	0.3

a

b
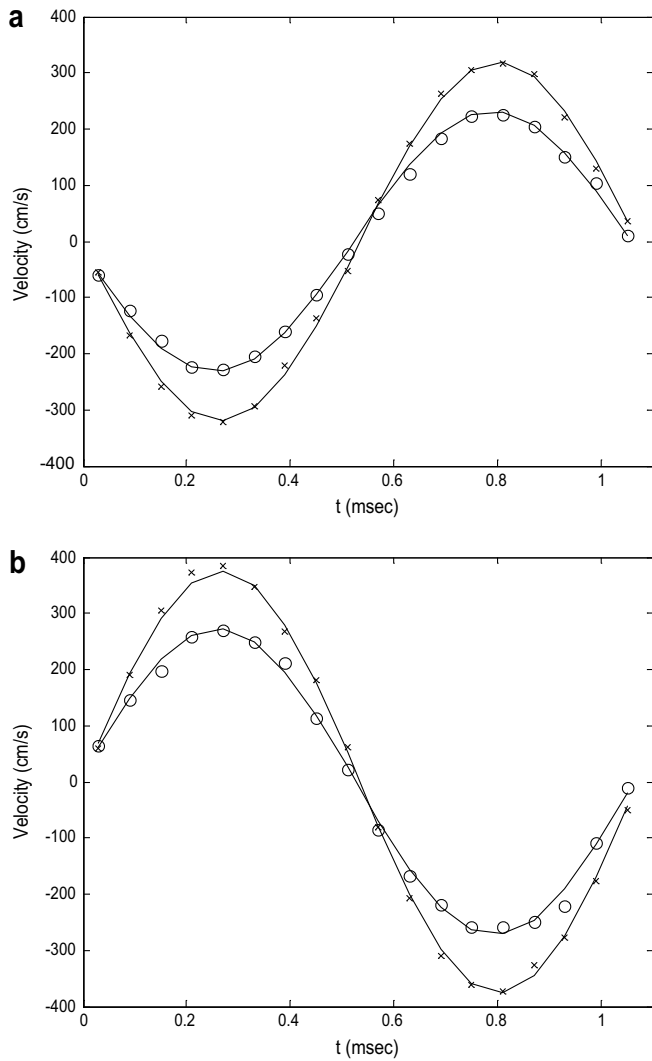
Fig. 6. Temporal variation of the experimental (symbols) and analytical (solid line) axial velocities for **a** $u_0 = 34$ cm/s ($\times$; $x = 3\lambda/4$, $\circ$; $x = 5\lambda/8$) and **b** $u_0 = 40$ cm/s ($\times$; $x = 5\lambda/4$, $\bigcirc$; $x = 9\lambda/8$).

Fig. 7. Spatial variation of the experimental axial velocities for $u_0 = 95$ cm/s at different phases, $\diamond$; $t/T = 0.25$, $*$; $t/T = 0.45$, $\circ$; $t/T=0.55$, $\times$; $t/T = 0.75$.

6. Conclusions

Spatial and temporal variations of the particle velocity inside an air-filled rigid-walled square channel in the presence of the quasi nonlinear standing waves are experimentally investigated. The synchronized PIV technique has been used to measure the acoustic velocity fields at 18 different phases over the excitation signal period for two different acoustic intensities. A good agreement between the experimental and analytical results in both time and space domains confirms the accuracy of the method. The analysis showed that the difference between the experimental and analytical values of axial velocity is on average less than 7.68%. The verified technique is then used to measure the acoustic velocity fields of the finite-amplitude nonlinear case at four different phases. The result shows a wavefront with high velocity gradient inside the resonator.

References

[1] V. Gusev, H. Bailliet, P. Lotton, M. Bruneau, Asymptotic theory of nonlinear acoustic waves in a thermoacoustic prime-mover, Acustica 86 (2000) 25–38.
[2] M. Akhavanbazaz, M.H.K. Siddiqui, R.B. Bhat, The impact of gas blockage on the performance of a thermoacoustic refrigerator, Experimental Thermal and Fluid Science 32 (2007) 231–239.
[3] Y.A. Ilinskii, B. Lipkens, T.S. Lucas, T.W. Van Doren, Nonlinear standing waves in an acoustical resonator, Journal of Acoustical Society of America 104 (1998) 2664–2674.
[4] Y. Roha, J. Kwon, Development of a new standing wave type ultrasonic linear motor, Sensors and Actuators A 112 (2004) 196–202.
[5] Y. Lee, J. Kwon, Separation and concentration of particles in fluid using ultrasonic standing wave, Key Engineering Materials 321 (2006) 63–66.
[6] A.B. Coppens, J.V. Sanders, Finite amplitude standing waves in rigid-walled tubes, Journal of Acoustical Society of America 43 (1968) 516–529.
[7] M. Bednařík, M. Červenka, Nonlinear waves in resonators, Nonlinear Acoustics at the Turn of Millennium 15 (2000) 165–168.
[8] B.O. Enflo, C.M. Hedberg, Theory of Nonlinear Acoustics in Fluids, Kluwer Academic Publishers, 2002.
[9] M.K. Aktas, B. Farouk, Numerical simulation of acoustic streaming generated by finite-amplitude resonant oscillations in an enclosure, Journal of Acoustical Society of America 116 (2004) 2822–2831.
[10] I. Christov, P.M. Jordan, C.I. Christov, Nonlinear acoustic propagation in homentropic perfect gases: a numerical study, Physics Letters A 353 (2006) 273–280.

Table 2
Percentage of the overall relative error (e_t) and the average of the standard deviation (mstd_t) in the temporal variation of the axial velocity over all 18 phases for cases A and B at two different locations

case A			case B		
x/λ	e_t (%)	mstd_t (cm/s)	x/λ	e_t (%)	mstd_t (cm/s)
3/4	4.26	1.7	5/4	4.30	1.9
5/8	5.04	1.8	9/8	6.32	2.2

also observed in the quasi-nonlinear cases (Figs. 4 and 5), although its value is smaller. The plot also shows a wavefront with high velocity gradient. The ratio between the positive and negative peaks of the wavefront changes with propagation. Such wavefront is not observed in the linear case. Thus, it can be concluded that for nonlinear standing waves, a wavefront with very high velocity and pressure gradients travels along the resonator.

Finally, the present study, for the first time, presents an accurate technique to measure the two-dimensional variations of the particle velocity inside the nonlinear standing wave resonator at different phase of the excitation signal.
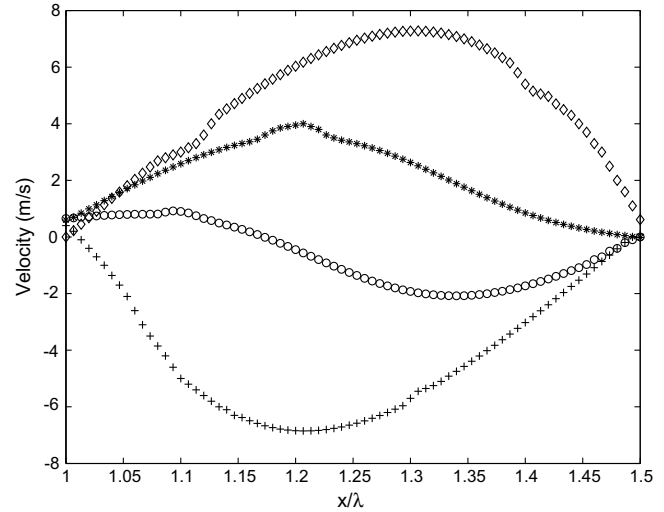
[11] C. Vanhille, C. Campos-Pozuelo, Numerical simulation of two-dimensional nonlinear standing waves, Journal of Acoustical Society of America 116 (2004) 194–200.

[12] C. Vanhille, C. Campos-Pozuelo, Three time-domain computational models for quasi-standing nonlinear acoustic waves, including heat production, Journal of Computational Acoustics 14 (2006) 143–156.

[13] M. Bednařík, M. Červenka, Nonlinear standing wave in 2D acoustic resonators, Ultrasonics 44 (2006) 773–776.

[14] L. Elvira-Segura, de Sarabia Riera-Franco, Numerical and experimental study of finite-amplitude standing waves in a tube at high sonic frequencies, Journal of Acoustical Society of America 104 (1998) 708–714.

[15] C. Vanhille, C. Campos-Pozuelo, Numerical and experimental analysis of strongly nonlinear standing acoustic waves in axisymmetric cavities, Ultrasonics 43 (2005) 652–660.

[16] G. Huelsz, F. Lopez-Alquicira, Hot-wire anemometry in acoustic waves, Experiments in Fluids 30 (2001) 283–285.

[17] G. Huelsz, F. Lopez-Alquicira, Velocity measurements in the oscillatory boundary layer produced by acoustic waves, Experiments in Fluids 32 (2002) 612–615.

[18] J.F. Vignola, Y.H. Berthelot, J. Jarzynski, Laser detection of sound, Journal of Acoustical Society of America 90 (1991) 1275–1286.

[19] M.W. Thompson, A.A. Atchley, Simultaneous measurement of acoustic and streaming velocities in a standing wave using lase Doppler anemometry, Journal of Acoustical Society of America 117 (2005) 1828–1838.

[20] B. Gazengel, S. Poggi, Measurement of acoustic particle velocities in enclosed sound field: assessment of two laser doppler velocimetry measuring systems, Applied Acoustics 66 (1) (2005) 15–44.

[21] Y.M.C. Delauré, V.S.S. Chan, D.B. Murray, A simultaneous PIV and heat transfer study of bubble interaction with free convection flow, Experimental Thermal and Fluid Science 27 (2003) 911–926.

[22] L. Martínez-Suastegui, C. Treviño, Particle image velocimetry measurements for opposing flow in a vertical channel with a differential and asymmetric heating condition, Experimental Thermal and Fluid Science 32 (2007) 262–275.

[23] D.B. Hann, C.A. Greated, Particle image velocimetry for the measurement of mean and acoustic particle velocities, Measurement Science and Technology 8 (1997) 656–660.

[24] D.B. Hann, C.A. Greated, The measurement of flow velocity and acoustic particle velocity using particle image velocimetry, Measurement Science and Technology 8 (1997) 1517–1522.

[25] M. Campbell, J.A. Cosgrove, C.A. Greated, J.D. Rockliff, Review of LDA and PIV applied to the measurement sound and acoustic streaming, Optics and Laser Technology 32 (2000) 629–639.

[26] Y. Shin, C. Jaewon, G.A. Domoto, C.P. Grigoropoulos, Compressible flow of liquid in a standing wave tube, Journal of Fluid Mechanics 536 (2005) 321–345.

[27] J.R. Castrejón-Pita, A.A. Castrejón-Pita, G. Huelsz, R. Tovar, Experimental demonstration of the Rayleigh acoustic viscous boundary layer theory, Physical Review E 73 (2005) 36601-1-5.

[28] M.H.K. Siddiqui, M.R. Loewen, C. Richardson, W.E. Asher, A.T. Jessup, Simultaneous particle image velocimetry and infrared imagery of microscale breaking waves, Physics of Fluids 13 (2001) 1891–1903.

[29] O.V. Rudenko, S.I. Soluyan, Theoretical Foundations of Nonlinear Acoustics, Consultants Bureau, New York, 1977.

[30] D.T. Blackstock, Fundamentals of Physical Acoustics, Wiley-Interscience publication, 2000.